Passivity-Oriented Design of LCL-type Grid-Connected Inverters with Luenberger Observer-based Active Damping

Zhao, Jiancheng; Xie, Chuan; Li, Kai; Zou, Jianxiao; Guerrero, Josep M.

Published in:
IEEE Transactions on Power Electronics

DOI (link to publication from Publisher):
10.1109/TPEL.2021.3109434

Publication date:
2022

Document Version
Accepted author manuscript, peer reviewed version

Citation for published version (APA):
Zhao, J., Xie, C., Li, K., Zou, J., & Guerrero, J. M. (2022). Passivity-Oriented Design of LCL-type Grid-Connected Inverters with Luenberger Observer-based Active Damping. *IEEE Transactions on Power Electronics*, *37*(3), 2625-2635. https://doi.org/10.1109/TPEL.2021.3109434

Passivity-Oriented Design of LCL-type Grid-Connected Inverters with Luenberger Observer-based Active Damping

Jiancheng Zhao, *Student Member, IEEE,* Chuan Xie, *Senior Member, IEEE,* Kai Li, *Member, IEEE,* Jianxiao Zou, *Member, IEEE,* and Josep M. Guerrero, *Fellow, IEEE*

***Abstract*—The frequency-domain passivity theory offers an effective way to assess the stability of inverters in a complex grid. In this paper, a unified impedance model, suitable for either inverter-current control (ICC) or grid-current control (GCC) of LCL-type grid-connected inverters (GCIs) with observer-based capacitor current feedback active damping (OAD), is built to facilitate the passivity-based stability assessment and controller parameter design. With the passivity analysis, it is found that when the anti-resonant frequency of LCL-filter is in certain ranges, *i.e.*, (0.056ω_s, 0.20ω_s) for ICC and (0.046ω_s, 0.23ω_s) for GCC, all frequencies' passive output admittance of the inverter can be achieved via proposed parameter design guidelines. Due to the utilization of the observer and all frequencies' passive output admittance property, not only extra current sensors for active damping can be saved, but also the inverter can be connected and stably operated in a grid regardless of the grid impedance. The validity of the theoretical analysis and effectiveness of the proposed method is verified by using experimental results on a laboratory prototype.**

***Index Terms*—voltage source inverter, observer-based active damping, LCL-filter, passivity, external stability, harmonic stability**

I. Introduction

The grid-connected inverters (GCIs) are very popular in renewable energy power systems, such as photovoltaic [1], wind turbines [2], energy storage [3], active power filter [4], *etc*. The proliferation of GCIs in the power grid would bring challenges to system stability, such as the harmonic stability issues that emerged in recent years [5]. The frequency-domain passivity-based control of GCIs emerges as a promising solution to mitigate harmonic instability caused by dynamic interactions between inverters and the power grid systems [5], [6]. By imposing a nonnegative-real-part in the closed-loop output admittance of GCI, *i.e.*, $Real\{Y(j\omega) \geq 0\}$ or $\angle Z(j\omega) \in [-90°, 90°], \forall\omega$, the GCI will not destabilize the connected electrical system [5].

An amount of research works have been devoted to the field of passivity evaluation and enhancement for GCIs [6]–[18]. It has been found that the computation and pulse width modulation (PWM) delays have significant effects on the passivity of the GCI [6]. Given the time delay of $1.5T_s$, for example, the one-sixth of the sampling frequency ($\omega_x = \omega_s/6$) was found as the critical frequency [7]. For the inverter-current-control (ICC) of LCL-type GCI, the negative-real-part region of GCI's output admittance is $(\omega_x, \omega_s/2)$ [7]–[9], where $\omega_s/2$ is the Nyquist frequency, while for the gird-current-control (GCC), the negative-real-part region of GCI's output admittance is between the ω_a and ω_x, where $\omega_a = \sqrt{1/(L_1 C_f)}$ which is the antiresonant frequency of the inverter-side inductance and filter capacitor of the LCL filter and could be either lower or higher than ω_x. For the passivity enhancement of the GCI's output admittance, the works can be categorized in two: one is reducing the time delay directly [10] or compensating for the time delay by the predictive method [11]–[13]; another is the virtual impedance method that in terms of inserting damping terms into the admittance (*e.g.*, passive or active damping method). For the ICC-GCI, Harnefors *et al.* proposed the grid voltage feedforward active damping plus capacitor-current feedback active damping (CCF-AD) to lift the non-negative-real-part region up to the Nyquist frequency [8]. However, an extra analog circuit-based high-pass filter is added and increases the cost as well as implementation complexity. For the GCC-GCI, the proportional-integral CCF-AD is proposed to enhance the overall non-negative-real-part region [14]. Whereas the negative-real-part region remains and still may trigger the system resonance. Akhavan *et al.* propose a biquad filter-based delay compensation method for CCF-AD to reshape the output admittance to be passive up to the Nyquist frequency [15]. Nevertheless, the biquad filter complicates the parameter selection and algorithm implementation. Xie *et al.* proposed a general admittance model based sub-admittance combination method, which achieved all frequencies' passivity of the output admittance suitable for both ICC-GCI and GCC-GCI. Nonetheless, current sensors used for CCF-AD are still required and will increase the system cost [9].

The observer can estimate the un-sampled state of the inverter to save the additional sensors. In paper [19], the Luenberger observer is used to save additional current sensors for the state space current controller. The extended-state observer is used to avoid using the voltage sensors in paper [20]. The sensorless current control solution relying on the Kalman

Manuscript received April 20, 2021; revised July 24, 2021; accepted August 29, 2021. This work was supported by the National Natural Science Foundation of China under Grant No. 51807021 and 61973054, and in part by Grant SCITLAB-0004 of Intelligent Terminal Key La-boratory of SiChuan Province and the VILLUM FONDEN under the VILLUM Investigator Grant (no. 25920): Center for Research on Microgrids (CROM). (*Corresponding author: Chuan Xie, Jiancheng Zhao*)

J. Zhao, C. Xie, K. Li and J. Zou are with the School of Automation Engineering, University of Electronic Science and Technology of China, Chengdu 611731, China (e-mail: zjclyc@qq.com; c.xie@uestc.edu.cn; kaili@uestc.edu.cn; jxzou@uestc.edu.cn).

J. M. Guerrero is with the Department of Energy Technology, Aalborg University, Aalborg 9220, Denmark (e-mail: joz@et.aau.dk).

This article has been accepted for publication in a future issue of this journal, but has not been fully edited. Content may change prior to final publication. Citation information: DOI 10.1109/TPEL.2021.3109434, IEEE Transactions on Power Electronics

filter is also proposed in the paper [21]. Although the Kalman filter can be described as a statistically optimal estimator, its drawback is that the process noise parameters are needed for tuning the observer [22]. The observer-based active damping (OAD) can successfully stabilize LCL-type GCI [16], [17], where additional current sensors are not required. However, it is known to be only valid for the inductive-impedance grid condition, and their effectiveness of stabilization in complex grid impedance conditions is unknown. In other words, the passivity property of the LCL-type GCI's output admittance with OAD yet has been studied.

In this paper, all frequencies' passive output admittance is achieved for both the converter-side and the grid-side current-controlled LCL-type grid-connected inverters by using a CCF-OAD without using additional current sensors. The system stability is guaranteed regardless of grid impedance value and the number of paralleled inverters. The main contributions can be summarized as follows.

1) A unified impedance model for both ICC-GCI and GCC-GCI with CCF-OAD to facilitate the passivity-based stability assessment and controller parameter design is derived in Section II.
2) In Section III, controller parameter design guidelines are given, and the passivity evaluation of GCI's output admittance is conducted. It is found that when the anti-resonant frequency of LCL-filter are in certain ranges, *i.e.*, $(0.056\omega_s, 0.20\omega_s)$ for ICC and $(0.046\omega_s, 0.23\omega_s)$ for GCC, all frequencies' passive output admittance of the GCI can be achieved.

The merits of the proposed method are as follow:

1) Thanks to all frequencies' passive output admittance of the inverter, it can be connected to a grid regardless of the grid impedance. Current sensors used for CCF-AD are saved for both the ICC-GCI and GCC-GCI.
2) As the method is elaborated in the stationary reference frame without coupling between the two axes, it is applicable for both the signal-phase and three-phase grid-connected voltage source inverters.

II. System Modelling and Analysis

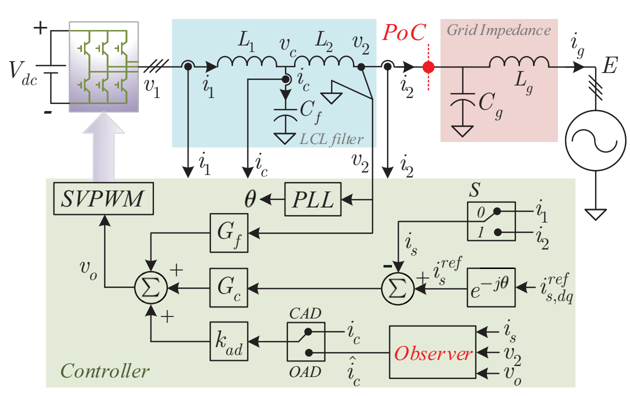

Fig. 1. Configuration of the studied three-phase GCI with an LCL filter.

Fig.1 shows the configuration of the studied three-phase grid-connected inverter (GCI) system with an LCL filter. In the figure, L_1, L_2, and C_f are the inverter-side inductor, grid-side inductor, and filter capacitor, respectively. L_g is the grid inductor, and C_g represents the power factor correction (PFC) capacitor connected at the point of coupling (PoC). The parasitic resistances of all inductors are neglected for the worst case with zero passive dampings [5]–[7].

For the control part, both the single-loop inverter-current-control (ICC, i_1) and grid-current-control (GCC, i_2) control objectives are considered. In addition, PoC voltage (v_2) is used as the inputs of the feedforward filter (G_f) and the phase lock loop (PLL). G_c is the phase-compensated proportional-resonant (PR) current controller implemented in the stationary $\alpha\beta$ reference frame, as shown in equation (1). The CCF-AD is also carried out to facilitate reshaping the output admittance of the GCI to be passive. Unlike the direct capacitor current feedback in [9], the capacitor current in this paper is obtained via a Luenberger observer, consequently, extra current sensors for capacitor currents can be saved and CCF-OAD is achieved.

$$G_c(s) = K_{cp} + K_{cr}\frac{s\cos\phi_1 - \omega_1\sin\phi_1}{s^2 + \omega_{rc}s + \omega_1^2} \tag{1}$$

where K_{cp}, K_{cr}, ω_1, ω_{rc}, and ϕ_1 are the proportional gain, resonant gain, resonant angular frequency, cutoff angular frequency, and compensation angle of the PR controller, respectively.

A. Model of the LCL Filter

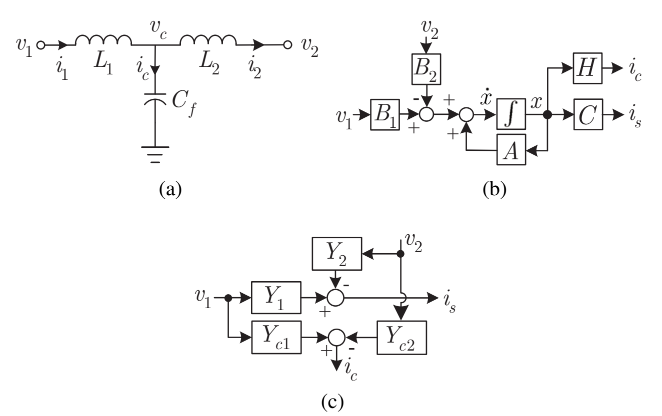

Fig. 2. (a) Circuit, (b) state-space and (c) s-domain model of the LCL filter.

For the LCL filter plant illustrated in Fig.2(a), the state variables are selected as $x = [i_1 \quad i_2 \quad v_c]^T$. The voltages v_1 and v_2 are the input of the plant; The currents i_1, i_2 and i_c are the selected outputs. Thus, the dynamics of the selected outputs can be represented in the state-space form as (2).

$$\begin{aligned}
\dot{x} &= \underbrace{\begin{bmatrix} 0 & 0 & -\frac{1}{L_1} \\ 0 & 0 & \frac{1}{L_2} \\ \frac{1}{C_f} & -\frac{1}{C_f} & 0 \end{bmatrix}}_{A} x + \underbrace{\begin{bmatrix} \frac{1}{L_1} \\ 0 \\ 0 \end{bmatrix}}_{B_1} v_1 - \underbrace{\begin{bmatrix} 0 \\ \frac{1}{L_2} \\ 0 \end{bmatrix}}_{B_2} v_2 \\
i_s &= \underbrace{\begin{bmatrix} (1-S) & S & 0 \end{bmatrix}}_{C} x \\
i_c &= \underbrace{\begin{bmatrix} 1 & -1 & 0 \end{bmatrix}}_{H} x
\end{aligned} \tag{2}$$

This article has been accepted for publication in a future issue of this journal, but has not been fully edited. Content may change prior to final publication. Citation information: DOI 10.1109/TPEL.2021.3109434, IEEE Transactions on Power Electronics

In the equation, the value of S in matrix C can be either 0 or 1, representing the ICC or GCC, respectively. ($i_s = i_1$ when $S = 0$, $i_s = i_2$ when $S = 1$). Thus, the unified s-domain model of the LCL filter can be achieved, as shown in (3) and (4).

$$i_s = \underbrace{C(sI - A)^{-1}B_1}_{Y_1} v_1 - \underbrace{C(sI - A)^{-1}B_2}_{Y_2} v_2 \tag{3}$$

and

$$i_c = \underbrace{H(sI - A)^{-1}B_1}_{Y_{c1}} v_1 - \underbrace{H(sI - A)^{-1}B_2}_{Y_{c2}} v_2 \tag{4}$$

B. Model of the Observer

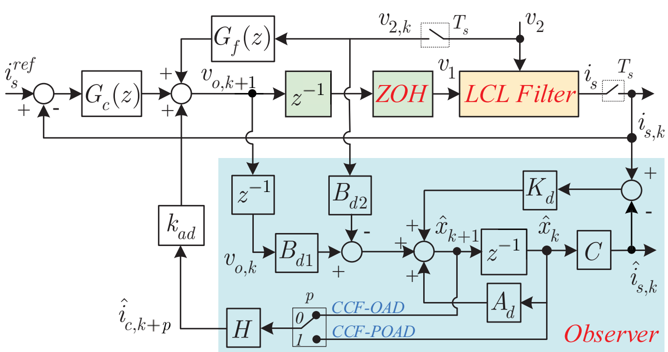

Fig. 3. Control block diagram of GCI with CCF-OAD in z-domain.

Fig.3 shows the control block diagram of GCI with CCF-OAD in z-domain. Since the observer is digitally implemented, the corresponding difference equation of the discrete observer is given in equation (5).

$$\begin{aligned} \hat{x}_{k+1} &= A_d\hat{x}_k + B_{d1}v_{o,k} - B_{d2}v_{2,k} + K_d(i_{s,k} - \hat{i}_{s,k}) \\ \hat{i}_{s,k} &= C\hat{x}_k \end{aligned} \tag{5}$$

where, A_d, B_{d1}, and B_{d2} is discretized from the A, B_1, and B_2, respectively, by using the zero-order-hold discretization method because of the equivalence between the PWM process and the zero-order-hold. T_s is the sampling period of the digital control, and K_d is the observer gain, which is designed by the pole placement method, as shown in appendix A.

As shown in Fig.3, the observed capacitor current could be with or without one-step prediction as follow:

$$\hat{i}_{c,k+p} = H\hat{x}_{k+p} \tag{6}$$

where, $p = 0, 1$.

Then, the model of the discrete observer in z-domain can be derived as:

$$\hat{i}_{c,k+p} = Y_{d1}(z)\, v_{o,k} - Y_{d2}(z)\, v_{2,k} + G_{dk}(z)\, i_{s,k} \tag{7}$$

where,

$$\begin{aligned} Y_{d1}(z) &= z^p H(zI - A_d + K_dC)^{-1}B_{d1} \\ Y_{d2}(z) &= z^p H(zI - A_d + K_dC)^{-1}B_{d2} \\ G_{dk}(z) &= z^p H(zI - A_d + K_dC)^{-1}K_d \end{aligned} \tag{8}$$

and $p = 0, 1$.

Although the observer is directly designed in the z-domain for higher precision of the digital system, the impedance model is inherently in the s-domain. For the impedance analysis compatiability, the z-domain observer model is transferred back to the s-domain by substituting z with e^{sT_s}, as shown in (9).

$$\hat{i}_c = Y_{d1}(s)\, v_o - Y_{d2}(s)\, v_2 + G_{dk}(s)\, i_2 \tag{9}$$

where,

$$\begin{aligned} Y_{d1}(s) &= e^{spT_s} H\left(e^{sT_s}I - A_d + K_dC\right)^{-1}B_{d1} \\ Y_{d2}(s) &= e^{spT_s} H\left(e^{sT_s}I - A_d + K_dC\right)^{-1}B_{d2} \\ G_{dk}(s) &= e^{spT_s} H\left(e^{sT_s}I - A_d + K_dC\right)^{-1}K_d \end{aligned} \tag{10}$$

C. Impedance Model of the GCI Seen from Sampling Position

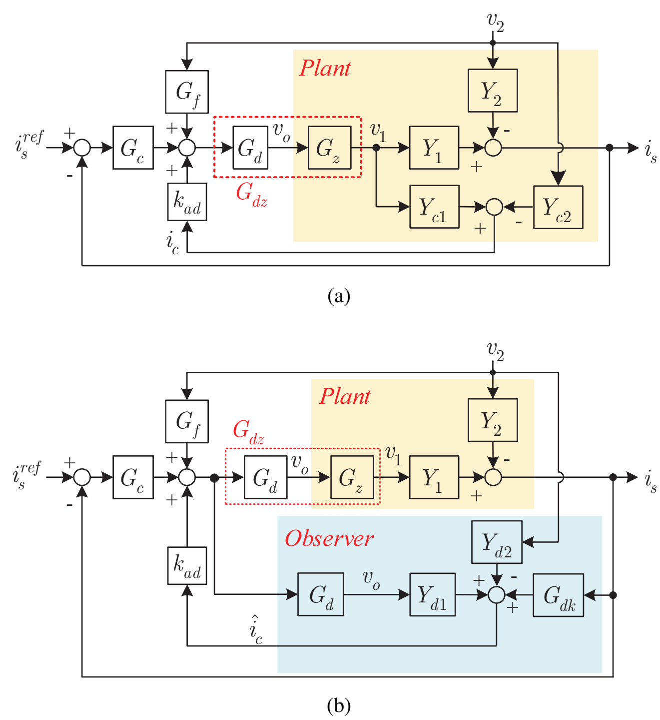

Fig. 4. Control block diagrams of GCI with (a) CCF-AD and (b) CCF-OAD in s-domain.

The impedance models of the GCI with CCF-AD and CCF-OAD are both depicted in Fig.4 for the sake of comparison. Since the single-side updated PWM is implemented in this paper, the time delay contains one sampling period of digital control delay G_d and a half sampling period of average PWM delay G_z. Thus, the total time delay is $1.5T_s$, as shown in (11). The parameter k_{PWM} is the proportional factor of the PWM, and $k_{PWM} = 1$, generally.

$$G_{dz}(s) = \underbrace{e^{-T_s s}}_{G_d} \underbrace{k_{PWM}\frac{1 - e^{-sT_s}}{sT_s}}_{G_z} \approx k_{PWM}e^{-1.5T_s s} \tag{11}$$

As shown in Fig.4, the output current of GCI seen from the sampling position can be expressed as (12).

$$i_s = G_i i_s^{ref} - Y_i v_2 \tag{12}$$

where, $G_i(s)$ and $Y_i(s)$ are the closed-loop transfer function and the equivalent output admittance for the GCI with CCF-AD, respectively. Applying Mason rules to the Fig.4(a) can result in

$$G_i(s) = \frac{G_c G_{dz} Y_1}{1 + G_c G_{dz} Y_1 - k_{ad} G_{dz} Y_{c1}} \tag{13}$$

$$Y_i(s) = \frac{\begin{pmatrix} Y_2\left(1 - k_{ad} G_{dz} Y_{c1}\right) \\ +k_{ad} Y_{c2} G_{dz} Y_1 - G_f G_{dz} Y_1 \end{pmatrix}}{1 + G_c G_{dz} Y_1 - k_{ad} G_{dz} Y_{c1}} \tag{14}$$

By contrast, for the GCI with CCF-OAD as shown in Fig.4(b), the corresponding closed-loop transfer function and the equivalent output admittance are

$$G_i(s) = \frac{G_c G_{dz} Y_1}{1 + G_c G_{dz} Y_1 - k_{ad}\left(G_d Y_{d1} + G_{dz} Y_1 G_{dk}\right)} \tag{15}$$

$$Y_i(s) = \frac{\begin{pmatrix} Y_2\left(1 - k_{ad} G_d Y_{d1}\right) \\ +k_{ad} Y_{d2} G_{dz} Y_1 - G_f G_{dz} Y_1 \end{pmatrix}}{1 + G_c G_{dz} Y_1 - k_{ad}\left(G_d Y_{d1} + G_{dz} Y_1 G_{dk}\right)} \tag{16}$$

D. Impedance Model of the GCI Seen from the PoC

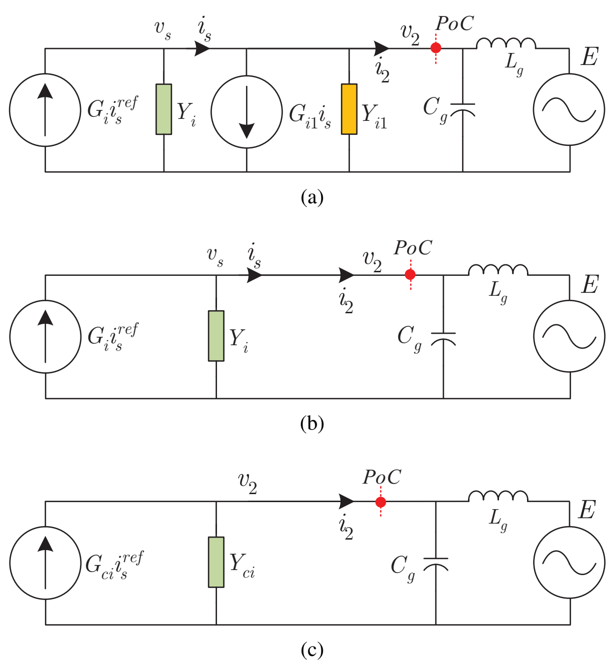

Fig. 5. The equivalent circuit of the (a) ICC-GCI, (b) GCC-GCI seen from the sampling position, and (c) the unified equivalent circuit seen from the PoC.

Combining (3), (4), (12) with the LC-type grid impedance adopted in Fig.1, the equivalent circuit for the overall system can be depicted as shown in Fig.5, in which Figs.5(a) and (b) are for GCC and ICC, respectively, and are unified in Fig.5(c). The grid current i_2 of the GCI seen from the PoC side can be represented as

$$i_2 = G_{ci} i_s^{ref} - Y_{ci} v_2 \tag{17}$$

where

$$G_{ci}(s) = S G_i + (1 - S)\left(1 - G_{i1}\right) G_i \tag{18}$$

$$Y_{ci}(s) = S Y_i + (1 - S)\left[(1 - G_{i1}) Y_i + Y_{i1}\right] \tag{19}$$

and, $G_{i1} = \frac{Y_{c1}}{Y_1}$, $Y_{i1} = \frac{Y_{c1} Y_2}{Y_1} - Y_{c2}$, $S = 0, 1$.

E. The Grid Impedance and Stability Criterion

According to Fig.5(c), the relationship between v_2 and E can be expressed as:

$$v_2 = \underbrace{\frac{s L_g}{1 + s^2 L_g C_g}}_{Z_g} i_2 + \underbrace{\frac{1}{1 + s^2 L_g C_g}}_{G_v} E \tag{20}$$

Substituting (20) into (17), the overall closed-loop current response seen from the E, which is the stiff grid voltage behind the grid impedance, can be derived as:

$$i_2 = \frac{G_{ci}}{1 + Y_{ci} Z_g} i_s^{ref} - \frac{Y_{ci} G_v}{1 + Y_{ci} Z_g} E \tag{21}$$

Equation (21) is equivalent to the circuit diagram, as shown in Fig.5(c). According to equation (21), the stable conditions of the whole system are:

1) G_{ci} has no right-half plane poles.
2) $Y_{ci} Z_g$ satisfies the Nyquist stabilization condition.

The first stability condition is called internal stability, which is determined by the poles of the current loop transfer function G_{ci} and has been extensively studied. The second stability condition is the external stability that represents the stability of the interaction between the GCI and the grid, which can be analyzed by applying the Nyquist criterion to the ratio of grid and GCI impedance, *i.e.*, $Y_{ci} Z_g$. However, if Z_g and Y_{ci} are both passive, then the second stability condition is guaranteed. As long as Z_g represents a resistive-inductive-capacitive (RLC) network, it is obviously passive. Remaining is, thus, to make Y_{ci} passive.

III. Controller Parameters Selection and Stability Analysis

A. Current Controller and Active damping Parameters Selection

An analytical parameter design guidelines for the current controller and CCF-AD parameters selection to realize all frequencies passive output admittance has been introduced in detail in [9]; It is cited here but with some minor modifications as follows.

For a current controller in (1), there are four parameters need to be tuned. With a given phase margin ϕ_m, typically set to be $(\pi/6, \pi/3)$, controller parameters can be calculated as

$$\begin{cases} \omega_c = \frac{\frac{\pi}{2} - \phi_m}{1.5 T_s} \\ K_{cp} = \omega_c L_1 \\ K_{cr} = \frac{K_{cp} \omega_c}{10} \\ \phi_1 = 1.5 \omega_1 T s \\ \omega_{rc} = 0.003 \end{cases} \tag{22}$$

The proportional gains for CCF-AD can be calculated as

$$k_{ad} = \left(\frac{\omega_a^2}{\omega_x^2} - S\right) k_{cp} \tag{23}$$

where, $\omega_a = \sqrt{(1/(L_1 C_f)}$, $\omega_x = 1/6\omega_x$. Then it will be demonstrated that the above design guidelines are still valid for CCF-OAD from the perspective of both internal and external system stabilities.

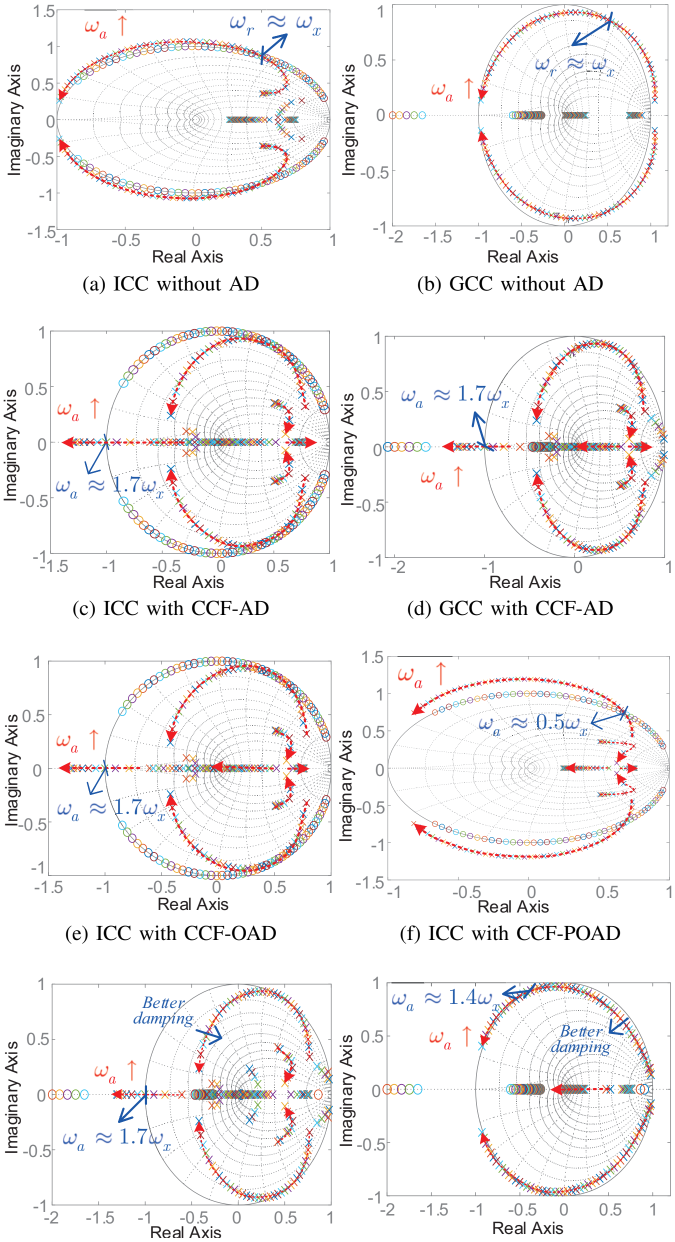

(a) ICC without AD (b) GCC without AD

(c) ICC with CCF-AD (d) GCC with CCF-AD

(e) ICC with CCF-OAD (f) ICC with CCF-POAD

(g) GCC with CCF-OAD (h) GCC with CCF-POAD

Fig. 6. Zeros and poles of G_i for various types of GCI and ω_a varies from $0.07\omega_x$ to $2.1\omega_x$.

B. Internal Stability for the GCI with OAD

The pole-zero map of G_i with ω_r varies from $0.1\omega_x$ to $3\omega_x$ are depicted in Fig.6. To figure out the different internal stability regions of the system for different conditions. As shown in Fig.6 (a) and (b), without CCF-AD, the stable regions for ICC and GCC are respectively $\omega_r < \omega_x$ and $\omega_r > \omega_x$, where ω_r is the resonant frequency of LCL filter and poles of G_i locates inside the unit circle. Note that this conclusion is in line with the one in [23], [24]. When CCF-AD is enabled with parameters given in (23), the poles of G_i locate inside the unit circle in case that $\omega_a < 1.7\omega_x$ as shown in Fig.6 (c) and (d), which means that the internal stability is ensured regardless of the location of ω_r, which agrees with the conclusion in [9]. When CCF-AD is replaced by the CCF-OAD and both without and with one-step prediction are considered. Note that observers without or with one-step prediction are respectively denoted as OAD and POAD briefly. The stable regions for CCF-OAD and CCF-POAD for ICC and GCC are respectively figured out from Fig.6 (e) to (h) and also listed in Table I, according to which, the following conclusions can be made:

1) Compared with CCF-AD, the CCF-OAD almost hasn't changed the internal stability regions for both ICC and GCC.
2) CCF-POAD shrank sharply the internal stability regions for ICC but, only a little for GCC.

Considering the sharp shrinkage of the internal stability regions of CCF-POAD for ICC, which is not recommended. Although the stable range of CCF-POAD is smaller than the CCF-OAD for GCC, yet the CCF-POAD is recommend because of the constraints of the output admittance's passivity which will be further explained in the next section.

TABLE I
INTERNAL STABLE REGIONS FOR CCF-OAD AND CCF-POAD

	ICC	GCC
CCF-OAD	$\omega_a < 1.7\omega_x$	$\omega_a < 1.7\omega_x$
CCF-POAD	$\omega_a < 0.5\omega_x$	$\omega_a < 1.4\omega_x$

C. Passivity for the GCI with CCF-OAD or CCF-POAD

By set G_f to 0, the $Real\{Y_{ci}(j\omega)\}$ of the GCI with CCF-AD are in the first place plotted in Fig.7 for the sake of comparison and validation of the correctness of the admittance model. It can be seen from the figure all frequencies' passive output admittance are achieved for both ICC and GCC with CCF-AD regardless of ω_a, which complies with the conclusion in [9] and validates the correctness of the admittance model.

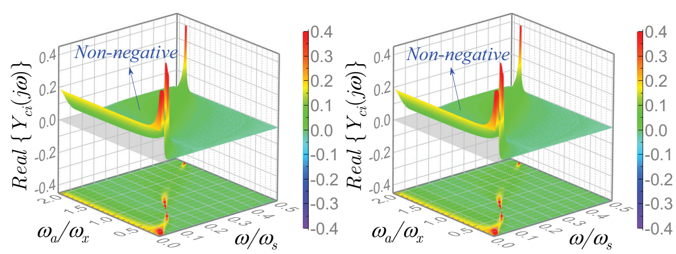

(a) ICC with CCF-AD (b) GCC with CCF-AD

Fig. 7. $Real\{Y_{ci}(j\omega)\}$ that neglecting the feedforward filter ($G_f = 0$) and ω_a varies from $0.07\omega_x$ to $2.1\omega_x$.

Then, $Real\{Y_{ci}(j\omega)\}$ of GCI are plotted in Fig.8. for four different conditions, *i.e.*, ICC with CCF-OAD and CCF-POAD, GCC with CCF-OAD and CCF-POAD, it can be seen that negative regions appeared which indicates the deterioration of the output admittance's passivity. Nevertheless, the negative $Real\{Y_{ci}(j\omega)\}$ in the high-frequency range can be compensated by the voltage feedforward which will be demonstrated in the next section. Meanwhile, the positive $Real\{Y_{ci}(j\omega)\}$ near the critical frequency, *i.e.*, ω_x will co-incidently correct the negative $Real\{Y_{ci}(j\omega)\}$ induced by the

This article has been accepted for publication in a future issue of this journal, but has not been fully edited. Content may change prior to final publication. Citation information: DOI 10.1109/TPEL.2021.3109434, IEEE Transactions on Power Electronics

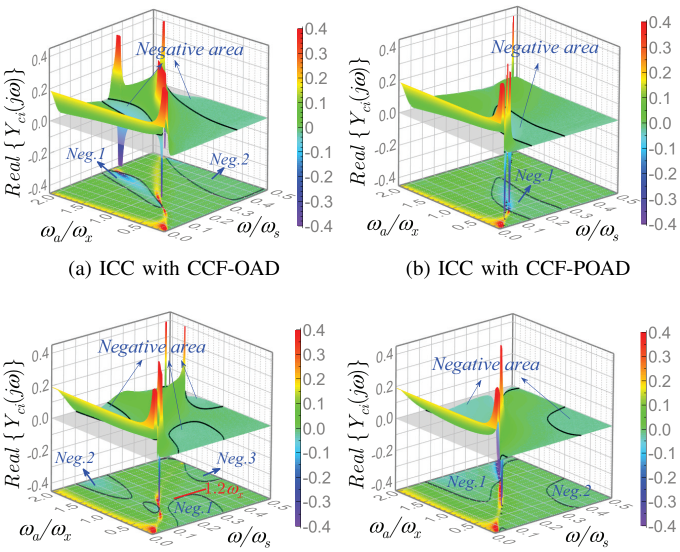

(a) ICC with CCF-OAD (b) ICC with CCF-POAD

(c) GCC with CCF-OAD (d) GCC with CCF-POAD

Fig. 8. $Real\{Y_{ci}(j\omega)\}$ of the GCI with OAD that neglecting the feedforward filter ($G_f = 0$) and ω_a varies from $0.07\omega_x$ to $2.1\omega_x$.

voltage feedforward as shown in Fig.9. According to Fig.8 and 9, the characteristics of output admittance for ICC with CCF-OAD and GCC with CCF-POAD satisfy these requirements. It also answered the question why the CCF-POAD rather than CCF-OAD is recommended for GCC that been posted in the previous section.

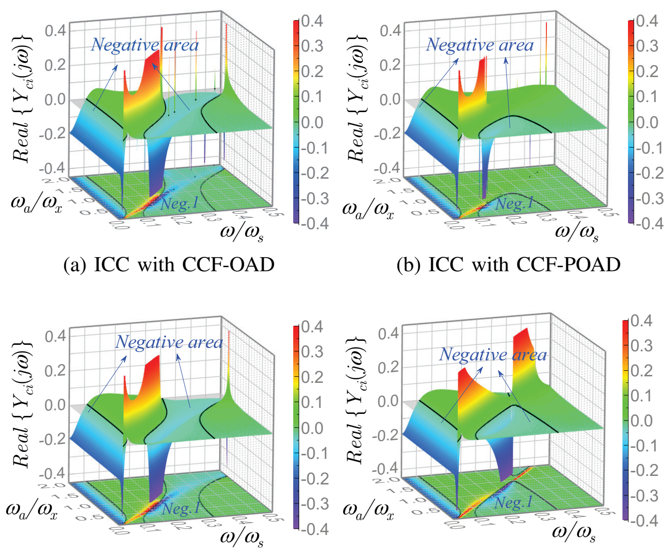

(a) ICC with CCF-OAD (b) ICC with CCF-POAD

(c) GCC with CCF-OAD (d) GCC with CCF-POAD

Fig. 9. $Real\{Y_{ci,f}(j\omega)\}$ (the admittance that related to the feedforward part) and ω_a varies from $0.07\omega_x$ to $2.1\omega_x$ ($k_f = 1$).

D. Passivity of the GCI plus Voltage Feedforward

For the objectives of inrush current suppression at startup process as well as output admittance reshaping, the voltage feedforward that consists of a proportional term and band-pass filter with unit gain at the fundamental frequency and adjustable gain is adopted in this paper, which is the form of

$$G_f(s) = k_f + (1 - k_f)\frac{\alpha_f (s\cos\phi_2 - \omega_1 \sin\phi_2)}{s^2 + \alpha_f s + \omega_1^2} \quad (24)$$

where k_f is the voltage feedforward gain, α_f and ϕ_2 are the cutoff frequency and phase-lead angular of the bandwidth filter, respectively. α_f is typically set to be a small value, *e.g.*, $\alpha_f = 0.01\omega_s$, ϕ_2 is set to compensate the phase-lag at the grid frequency ω_1, *i.e.*, $\phi_2 = 1.5\omega_1 T_s$.

The admittance with respect to the voltage feedforward can be split out from (18) for further passivity-oriented parameter selection for the voltage feedforward. The corresponding admittance can be expressed as

$$Y_{i,f}(s) = \frac{-G_f G_{dz} Y_1}{1 + G_c G_{dz} Y_1 - k_{ad}(G_d Y_{d1} + G_{dz} Y_1 G_{dk})} \quad (25)$$

Replacing $Y_i(s)$ in (21) with $Y_{i,f}(s)$, the feedforward corresponding admittance seen from the PoC can be achieved, which is denoted by $Y_{ci,f}(s)$ and its real part is drawn in Fig.9. It can be seen that the passivity properties of the voltage feedforward related output admittance are complementary with that of the current control loop. *i.e.*, Fig.8(a) with Fig.9(a) and Fig.8(d) with Fig.9(d). Hence, by the appropriate selection of feedforward gain, all frequencies passive output admittance can be achieved. It can also be seen that there are overlapping negative real part regions in Fig.8(b) and Fig.9(b) as well as Fig.8(c) with Fig.9(c), all frequencies' passive output admittance are definitely not achieveable, this is the reason why CCF-POAD and CCF-OAD are not recommended for ICC and GCC, respectively.

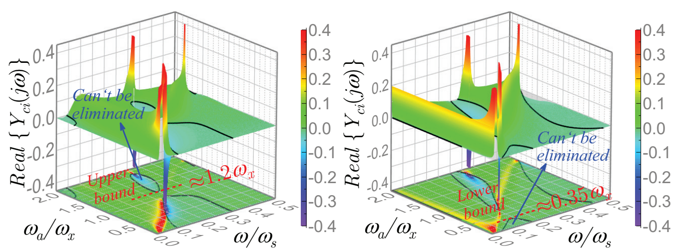

(a) $k_f = 1$ (b) $k_f = 0$

Fig. 10. $Real\{Y_{ci}(j\omega)\}$ for the ICC with the CCF-OAD and ω_a varies from $0.07\omega_x$ to $0.21\omega_x$.

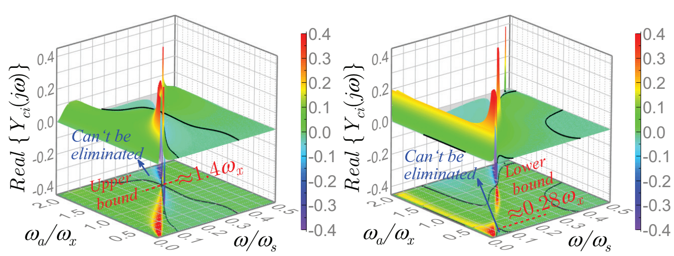

(a) $k_f = 1$ (b) $k_f = 0$

Fig. 11. $Real\{Y_{ci}(j\omega)\}$ for the GCC with the CCF-POAD and ω_a varies from $0.07\omega_x$ to $0.21\omega_x$.

Then, the $Real\{Y_{ci}(j\omega)\}$ for ICC with CCF-OAD and GCC with CCF-POAD plus feedforward are drawn in Fig.10 and Fig.11, respectively. Then, the boundaries for realization of all frequencies' passive output admittance for the CSC-OAD and CSC-POAD are roughly refined out:

- ICC with CCF-OAD: $0.056\omega_s \approx 0.35\omega_x < \omega_a < 1.2\omega_x \approx 0.20\omega_s$
- GCC with CCF-POAD: $0.046\omega_s \approx 0.28\omega_x < \omega_a < 1.4\omega_x \approx 0.23\omega_s$

IV. Experimental Verification

For validating the correctness of the theoretical analysis and the effectiveness of the proposed controller parameter design method, an experimental setup is built up in the laboratory as shown in Fig.12. The setup consists of four three-phase inverters with LCL filters, one of them is performed as the grid-connected inverter under test. The control algorithm is implemented in the dSPACE 1005 platform for real-time control. The power stage parameters are listed in Table II for the controller parameters design. Without loss of generality, two cases with the resonant frequencies of LCL-filter either beyond (Case 1: $C_f = 9.8\mu F$) or below (Case 2: $C_f = 24.8\mu F$) the critical frequency, *i.e.*, ω_x, are considered.

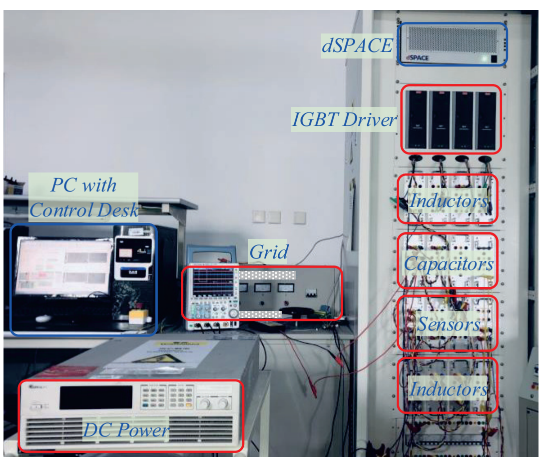

Fig. 12. Hardware picture for the experimental setup.

In this paper, the open-loop phase margin ϕ_m is set to $15\pi/36$ radians (75 degrees). Then, the current controller parameters as well as the proportional gains for CCF-AD can be analytically calculated according to (22) and (23), respectively, and the resultant are listed in Table II.

The voltage feedforward gains can be graphically determined by plotting curves of $Real\{Y_{ci}(j\omega)\}$. Fig.13 shows the curves of $Real\{Y_{ci}(j\omega)\}$ for different cases with k_f varies from 0 to 1. As see in Fig.13, for both control objectives, *i.e.*, ICC or GCC, and for both cases, an appropriate k_f can be graphically found out to realize all frequencies' passive output admittance. The specific values of k_f used in experiments for different cases are also listed in Table II.

Since the observer depends on the parameters of the LCL filter, *i.e.*, converter-side inductance (L_1), grid-side inductance (L_2), and the capacitance (C_f). The influence of variations of those parameters on the passivity of the inverter output admittance is analyzed. According to Fig.13, for either ICC or GCC, case one exhibits a relatively poor overall passivity for output admittance, hence only case one is analyzed. According to Fig.14, for ICC with CCF-OAD, all frequencies passive output admittance can be ensured if the inductor and filter capacitor of the LCL filter have tolerances of $(-30\%, 8\%)$ and $(-28\%, 5\%)$, respectively. Fig.15 shows that GCC with CCF-POAD has a wider allowable tolerance of power stage parameters than that of ICC with CCF-OAD.

Before conducting experiments, theoretical stability assessments are performed by using Bode plots of both inverter

TABLE II
Controller Parameters

Power Stage Parameters				
Parameters			Values	
LCL filter converter-side inductance (L_1)			1.4mH	
LCL filter grid-side inductance (L_2)			1.4mH	
LCL filter capacitance(C_f)			9.8μF / 24.8μF	
Grid frequency (f_1/ω_1)			50Hz/100π	
Grid voltage (Ph-Ph) (E_{rms})			150V	
Direct voltage (V_{dc})			350V	
Common Parameters				
Parameters			Values	
Sampling period/frequency (T_s/f_s)			1e-4s/10kHz	
Feedforward Filter cutoff frequency (α_f)			100π	
PR controller (α_c)			$0.03\omega_s$	
PR controller (k_{cr})			500	
PR controller (ω_c)			π	
Observer dominant frequency (ω_d)			$0.5\omega_s$	
Observer damping factor (ζ)			0.707	
Particular Parameters				
Types of GCI	Case 1: $\omega_a = 0.85\omega_x$		Case 2: $\omega_a = 0.5\omega_x$	
	k_{ad}	k_f	k_{ad}	k_f
ICC-OAD	$0.66k_{cp}$	0.2	$0.26k_{cp}$	0.05
GCC-POAD	$-0.34k_{cp}$	0.4	$-0.74k_{cp}$	0.5

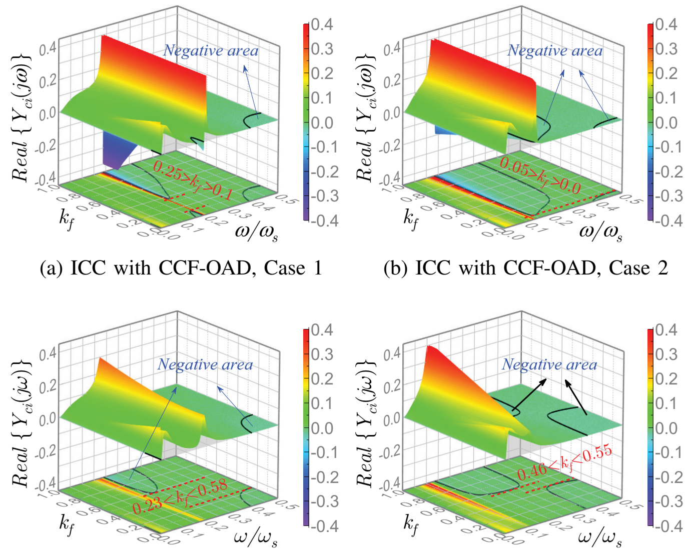

(a) ICC with CCF-OAD, Case 1 (b) ICC with CCF-OAD, Case 2
(c) GCC with CCF-POAD, Case 1 (d) GCC with CCF-POAD, Case 2

Fig. 13. $Real\{Y_{ci}(j\omega)\}$ of the GCC type GCI (k_f varies from 0.0 to 1.0).

This article has been accepted for publication in a future issue of this journal, but has not been fully edited. Content may change prior to final publication. Citation information: DOI 10.1109/TPEL.2021.3109434, IEEE Transactions on Power Electronics

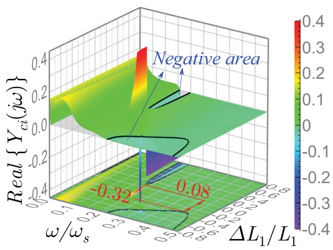

(a) L_1 variation

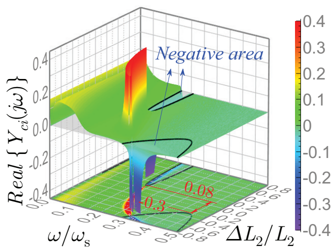

(b) L_2 variation

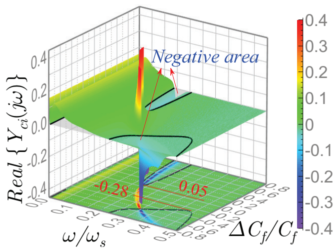

(c) C_f variation

Fig. 14. $Real\{Y_{ci}(j\omega)\}$ of the ICC with CCF-OAD type GCI with the LCL parameters variation (Case 1, *i.e.*, $\omega_a = 0.5\omega_x$, $k_f = 0.05$).

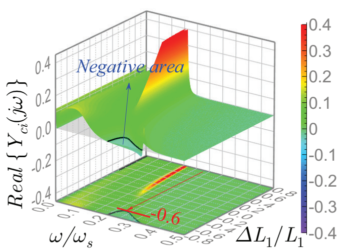

(a) L_1 variation

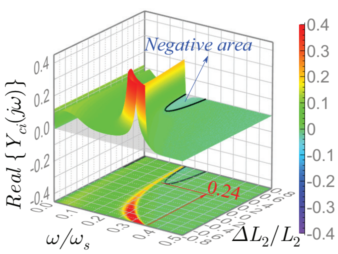

(b) L_2 variation

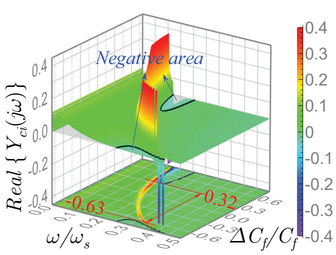

(c) C_f variation

Fig. 15. $Real\{Y_{ci}(j\omega)\}$ of the GCC with CCF-POAD type GCI with the LCL parameters variation (Case 1, *i.e.*, $\omega_a = 0.5\omega_x$, $k_f = 0.5$).

output admittance and grid admittance. Normally, the stability in terms of PM can be interpreted by the phase difference at the intersection point of the magnitude responses of the inverter output admittance and grid admittance [25], [26], viz., the phase difference over 180 degrees indicates instability and vice versa. Since the passive output admittance in all frequencies is achieved with the proposed method, viz., the system stability is ensured regardless of the intersection locations of the magnitude responses of the inverter output admittance and grid admittance. When disabling the proposed method, negative-real-part regions of the output admittance appear, at where if the intersection locations of the magnitude responses of the inverter output admittance and grid admittance occurring may lead to the system instability. In this paper, the LC-type resonant circuit is used to simulate the grid impedance (see in Fig.1) to build the instability conditions intentionally.

A. Passivity-based Stability Verification for the ICC with CCF-OAD type GCI

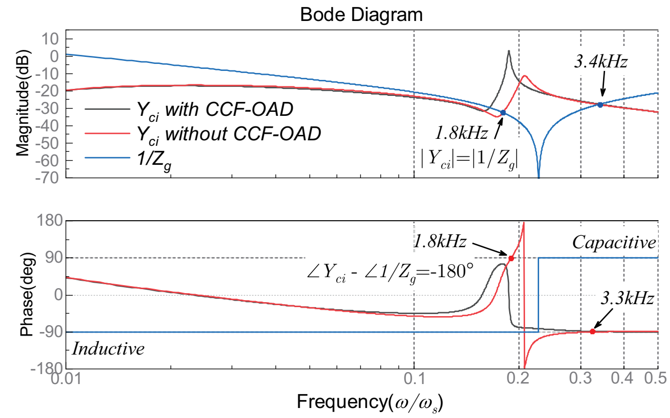

Fig. 16. Resonant analyze of the ICC-GCI with CCF-OAD where $\omega_a = 0.85\omega_x$ (Case 1 with $L_g = 1.4mH$ and $C_g = 3.5\mu F$).

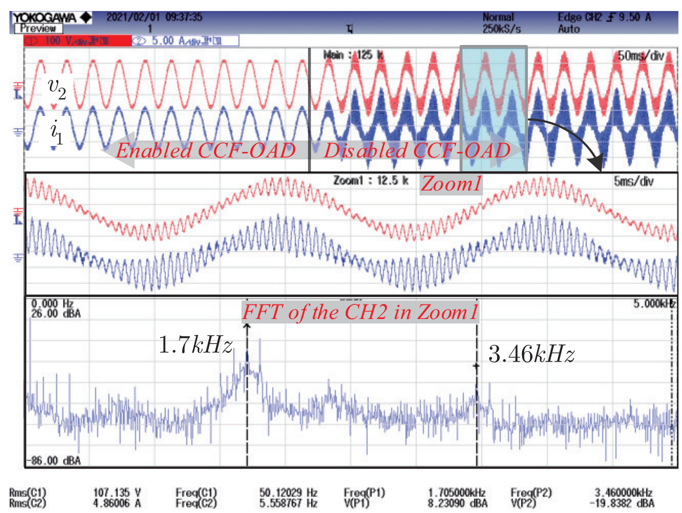

Fig. 17. Experiment results of ICC-GCI with CCF-OAD where $\omega_a = 0.85\omega_x$ (Case 1 with $L_g = 1.4mH$ and $C_g = 9.8\mu F$).

Fig.16 shows the bode diagram of the admittance for the VSC with the LCL parameter in case 1 and the grid admittance $1/Z_g$. For the GCC without active damping, the system has two possible resonant frequencies (*i.e.*, 1.8kHz and 3.3kHz). Fig.17 shows the experimental result corresponding to the senario in Fig.16. The inverter-side current (i_1) is stable for the GCI with CCF-OAD. However, the current becomes to resonant when the CCF-OAD is turnoff (Without AD). The real-time fast Fourier transform (FFT) of the resonant current shows that the experimental resonant frequency are $1.7kHz$ and $3.46kHz$. The experimental results is consistent with the theoretical analysis in Fig.16.

This article has been accepted for publication in a future issue of this journal, but has not been fully edited. Content may change prior to final publication. Citation information: DOI 10.1109/TPEL.2021.3109434, IEEE Transactions on Power Electronics

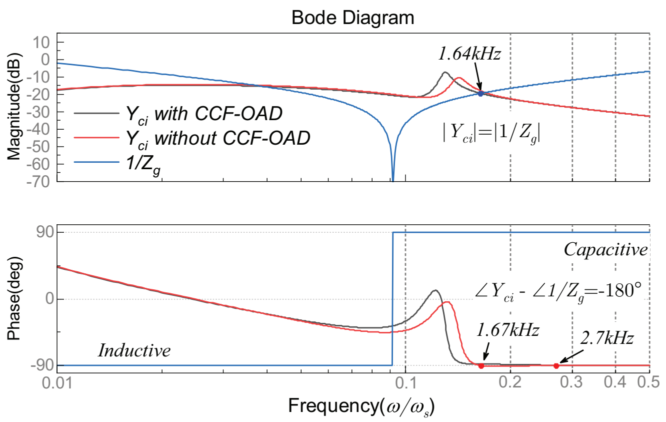

Fig. 18. Resonance analyze of the ICC-GCI with CCF-OAD where $\omega_a = 0.5\omega_x$ (Case 2 with $L_g = 2.0mH$ and $C_g = 15.0\mu F$).

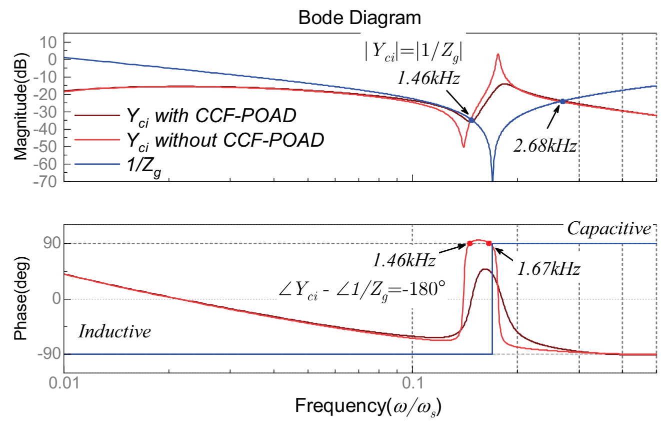

Fig. 20. Resonance analyze of the GCC-GCI with CCF-POAD where $\omega_a = 0.85\omega_x$ (Case 1 with $L_g = 1.4mH$ and $C_g = 6.3\mu F$).

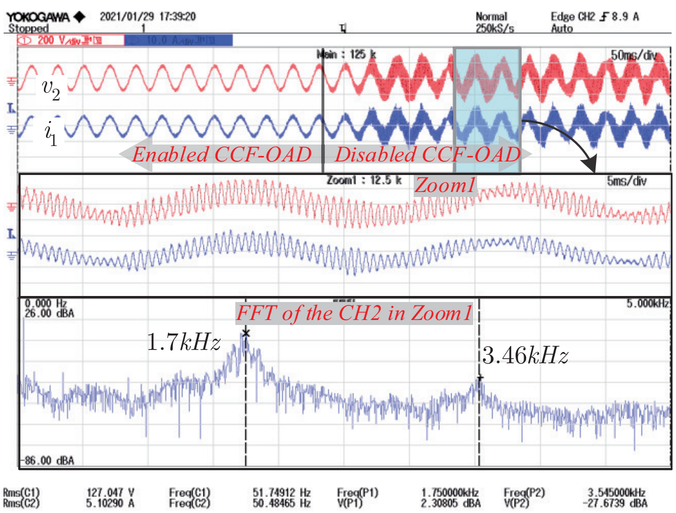

Fig. 19. Experiment results for the ICC-GCI with CCF-OAD where $\omega_a = 0.5\omega_x$ (Case 2 with $L_g = 2.0mH$ and $C_g = 15.0\mu F$).

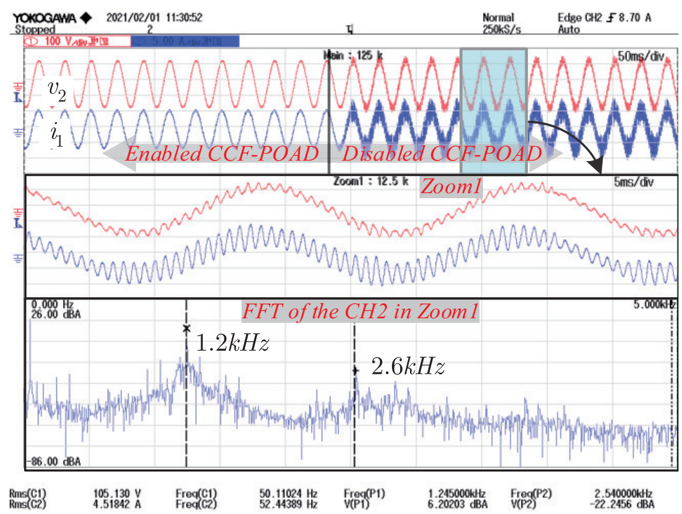

Fig. 21. Experimental results of the GCC-GCI with CCF-POAD where $\omega_a = 0.85\omega_x$ (Case 1 with $L_g = 1.4mH$ and $C_g = 6.3\mu F$).

Fig.18 shows admittances for the ICC-CCF-OAD with power stage parameters in case 2. For the GCC without active damping, the possible resonant frequency of the system is 1.67kHz. Fig.19 shows the experimental results corresponding to the senario in Fig.18. The system is stable with the proposed CCF-OAD, but is resonant at $1.7kHz$ when the CCF-OAD is disabled. The experimental result agrees with the theoretical analysis.

B. Passivity-based Stability Verification for the GCC with CCF-POAD type GCI

Fig.20 shows the bode diagram of the admittance for the GCC with CCF-POAD type GCI with LCL parameters in case 1. There are two possible resonant frequencies for the GCI without active damping, which are 1.47kHz and 2.68kHz. Fig.21 is the experimental result corresponding to the senario in Fig.20. The real resonant frequency is $1.2kHz$ and $2.6kHz$. There is a small deviation between the experimental and theoretical analytical results.

Fig.22 shows the bode diagram of the admittance for the GCC-CCF-POAD type GCI with LCL parameters in case 2. For the VSC without active damping, the system may be resonant at the high frequencies. And the possible resonant frequencies are $0.91kHz$ and $1.67kHz$. Fig.23 shows the experimental results corresponding to Fig.22. According to the FFT analysis result, the real resonant frequency are $0.96kHz$ and $1.96kHz$. And the system is stable with the proposed CCF-POAD method.

V. Conclusion

This paper builds a unified impedance model for both inverter current control (ICC) and grid-current control (GCC) LCL-type grid-connected inverters (GCIs) with observer-based capacitor current feedback active damping (CCF-OAD). After the passivity assessment and controller parameter optimization, it is found that when the antiresonant frequency of LCL-filter are in certain ranges, *i.e.*, $(0.056\omega_s, 0.20\omega_s)$ for ICC and $(0.046\omega_s, 0.23\omega_s)$ for GCC, all frequencies' passive output admittance of the GCI can be achieved under the proposed controller parameters design guidelines. And one-step prediction of the observer is required for GCC to ensure all frequencies' passive output admittance, while it is yet not

This article has been accepted for publication in a future issue of this journal, but has not been fully edited. Content may change prior to final publication. Citation information: DOI 10.1109/TPEL.2021.3109434, IEEE Transactions on Power Electronics

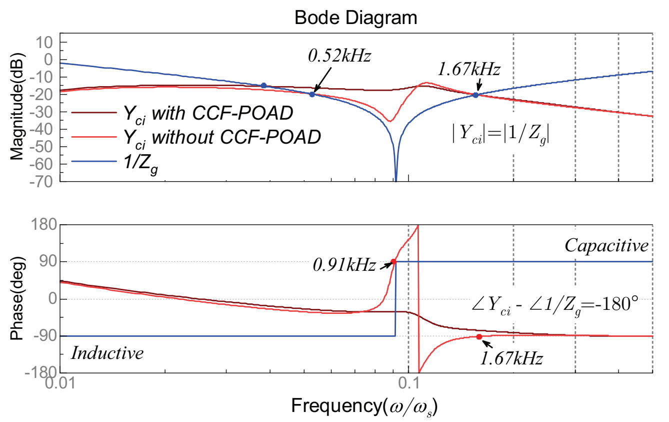

Fig. 22. Resonance analyze of the GCC-GCI with CCF-POAD where $\omega_a = 0.5\omega_x$ (Case 2 with $L_g = 2.0mH$ and $C_g = 15.0\mu F$).

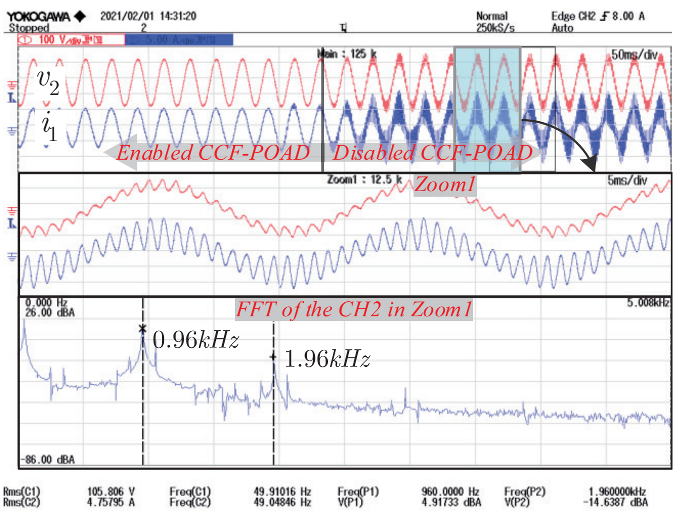

Fig. 23. Experiment results of the GCC-GCI with CCF-POAD where $\omega_a = 0.5\omega_x$ (Case 2 with $L_g = 2.0mH$ and $C_g = 15.0\mu F$).

needed for ICC. In addition, it is also found that GCC with CCF-POAD has a wider allowable tolerance of power stage parameters than that of ICC with CCF-OAD.

Appendix A
The Pole Placement of the Observer

The closed-loop poles of the observer can be selected according to the open-loop poles of the plant, which are roots of the plant's characteristic equation (2), *i.e.*, $|sI - A| = s(s^2 + \omega_r^2)$, where ω_r is the resonant frequency of the LCL filter. There are three open-loop poles, two complex conjugate poles (the resonant poles) at the resonant frequency and a real pole at zero frequency. In order to achieve a fast and damped response observer, the pole at zero frequency is moved to a higher frequency and the resonant poles are damped with factor ζ (typically, $\zeta = 0.7$ is used) [27], which gives three closed-loop poles as

$$\begin{aligned} p_{s0} &= -\omega_d \\ p_{s1} &= -\omega_r(\zeta - j\sqrt{1-\zeta^2}) \\ p_{s1}^* &= -\omega_r(\zeta + j\sqrt{1-\zeta^2}) \end{aligned} \tag{26}$$

Then, the above s-domain poles are mapped into z-domain with the relationship $z = e^{sT_s}$, which gives

$$\begin{aligned} p_{z0} &= e^{-\omega_d T_s} \\ p_{z1} &= e^{-\omega_r\left(\zeta - j\sqrt{1-\zeta^2}\right)T_s} \\ p_{z1}^* &= e^{-\omega_r\left(\zeta + j\sqrt{1-\zeta^2}\right)T_s} \end{aligned} \tag{27}$$

Finally, the characteristic equation of the discrete observer is derived as:

$$|zI - A_d + K_d C| = (z - p_{z0})(z - p_{z1})(z - p_{z1}^*) \tag{28}$$

where the observer gain K_d can be achieved by using the MATLAB command $place()$.

$$K_d = [k_{d1} \quad k_{d2} \quad k_{d3}]^T = place(A_d', C', [p_{z0} \quad p_{z1} \quad p_{z1}^*])'$$

The performance of the observer is dominated by its dominant pole, *i.e.*, p_{z0}, to be more intuitive, the Bode plots for the error transfer function of the observer (29) with the dominant pole at different frequencies are plotted in Fig.24.

$$e_{is} = \frac{\hat{i}_s - i_s}{i_s} = 1 - C(zI - A_d + K_d C)^{-1} K_d \tag{29}$$

It can be seen from Fig.24, a high frequency of the dominant pole p_{z0} leads to smaller observer error, which is desired for the capacitor current feedback active damping (CCF-AD) and inverter output admittance reshaping. However, further increasing the frequency of the dominant pole beyond nyqusit frequency will no long improve the accuracy of the observer. Hence, the frequency of the dominant pole of the observer is recommended to be set as the Nyquist frequency.

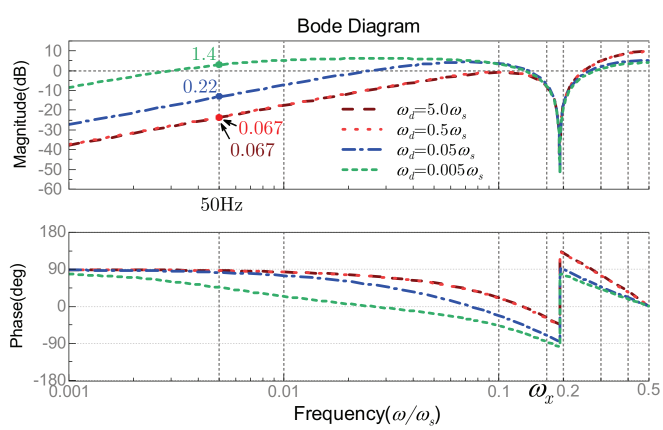

Fig. 24. The stable tracking error of the observer for the ICC-GCI with CCF-OAD where and $\omega_a = 0.85\omega_x$.

This article has been accepted for publication in a future issue of this journal, but has not been fully edited. Content may change prior to final publication. Citation information: DOI 10.1109/TPEL.2021.3109434, IEEE Transactions on Power Electronics

REFERENCES

[1] K. Alluhaybi, I. Batarseh, and H. Hu, "Comprehensive review and comparison of single-phase grid-tied photovoltaic microinverters," *IEEE J. Emerg. Sel. Top. Power Electron.*, vol. 8, no. 2, pp. 1310–1329, Jun. 2020.

[2] F. Blaabjerg and K. Ma, "Wind energy systems, reviews application of power electronics in wind energy systems," *IEEE Power Energy Soc.*, vol. 105, no. 11, pp. 2116–2131, 2017.

[3] M. Faisal, M. A. Hannan, P. J. Ker, A. Hussain, M. B. Mansor, and F. Blaabjerg, "Review of energy storage system technologies in microgrid applications: Issues and challenges," *IEEE Access*, vol. 6, pp. 35 143–35 164, 2018.

[4] C. Xie, X. Zhao, M. Savaghebi, L. Meng, J. M. Guerrero, and J. C. Vasquez, "Multirate fractional-order repetitive control of shunt active power filter suitable for microgrid applications," *IEEE J. Emerg. Sel. Top. Power Electron.*, vol. 5, no. 2, pp. 809–819, 2017.

[5] X. Wang and F. Blaabjerg, "Harmonic stability in power electronic-based power systems: Concept, modeling, and analysis," *IEEE Trans. Smart Grid*, vol. 10, no. 3, pp. 2858–2870, may 2019.

[6] L. Harnefors, X. Wang, A. G. Yepes, and F. Blaabjerg, "Passivity-based stability assessment of grid-connected VSCs—an overview," *IEEE J. Emerg. Sel. Top. Power Electron.*, vol. 4, no. 1, pp. 116–125, mar 2016.

[7] L. Harnefors, A. G. Yepes, A. Vidal, and J. Doval-Gandoy, "Passivity-based controller design of grid-connected VSCs for prevention of electrical resonance instability," *IEEE Trans. Ind. Electron.*, vol. 62, no. 2, pp. 702–710, feb 2015.

[8] L. Harnefors, L. Zhang, and M. Bongiorno, "Frequency-domain passivity-based current controller design," *IET Power Electron.*, vol. 1, no. 4, p. 455, 2008.

[9] C. Xie, K. Li, J. Zou, and J. M. Guerrero, "Passivity-based stabilization of LCL -type grid-connected inverters via a general admittance model," *IEEE Trans. Power Electron.*, vol. 35, no. 6, pp. 6636–6648, 2020.

[10] D. Yang, X. Ruan, and H. Wu, "A real-time computation method with dual sampling mode to improve the current control performance of the LCL-type grid-connected inverter," *IEEE Trans. Ind. Electron.*, vol. 62, no. 7, pp. 4563–4572, jul 2015.

[11] C. Chen, J. Xiong, Z. Wan, J. Lei, and K. Zhang, "A time delay compensation method based on area equivalence for active damping of an LCL-type converter," *IEEE Trans. Power Electron.*, vol. 32, no. 1, pp. 762–772, 2017.

[12] M. Lu, X. Wang, P. C. Loh, F. Blaabjerg, and T. Dragicevic, "Graphical evaluation of time-delay compensation techniques for digitally controlled converters," *IEEE Trans. Power Electron.*, vol. 33, no. 3, pp. 2601–2614, mar 2018.

[13] J. Zhao, K. Li, X. Wang, C. Xie, and H. Xu, "A novel passivity-based resonant instability suppression method for grid-connected VSC," *J. Electr. Eng. Technol.*, nov 2020.

[14] Y. He, X. Wang, X. Ruan, D. Pan, X. Xu, and F. Liu, "Capacitor-current proportional-integral positive feedback active damping for LCL -type grid-connected inverter to achieve high robustness against grid impedance variation," *IEEE Trans. Power Electron.*, vol. 34, no. 12, pp. 12 423–12 436, 2019.

[15] A. Akhavan, H. R. Mohammadi, J. C. Vasquez, and J. M. Guerrero, "Passivity-based design of plug-and-play current-controlled grid-connected inverters," *IEEE Trans. Power Electron.*, vol. 35, no. 2, pp. 2135–2150, 2020.

[16] V. Miskovic, V. Blasko, T. Jahns, A. Smith, and C. Romenesko, "Observer based active damping of LCL resonance in grid connected voltage source converters," in *2013 IEEE Energy Conversion Congress and Exposition*. IEEE, 9/15/2013 - 9/19/2013, pp. 4850–4856.

[17] B. Abdeldjabar, L. Huaiyuan, W. Jian, and X. Dianguo, "Robust observer based active damping control for LCL filtered grid connected converters using LMI criterion," in *2016 18th European Conference on Power Electronics and Applications (EPE'16 ECCE Europe)*. IEEE, 9/5/2016 - 9/9/2016, pp. 1–6.

[18] W. Wang, X. Gao, B. Fan, X. Zeng, and G. Yao, "Faulty phase detection method under single-line-to-ground fault considering distributed parameters asymmetry and line impedance in distribution networks," *IEEE Trans. Power Del.*, pp. 1–1, 2021.

[19] J. Kukkola and M. Hinkkanen, "Observer-based state-space current control for a three-phase grid-connected converter equipped with an LCL filter," *IEEE Trans. Ind. Appl.*, vol. 50, no. 4, pp. 2700–2709, jul 2014.

[20] B. Wang, Y. Xu, Z. Shen, J. Zou, C. Li, and H. Liu, "Current control of grid-connected inverter with LCL filter based on extended-state observer estimations using single sensor and achieving improved robust observation dynamics," *IEEE Trans. Ind. Electron.*, vol. 64, no. 7, pp. 5428–5439, jul 2017.

[21] K. Ahmed, A. Massoud, S. Finney, and B. Williams, "Sensorless current control of three-phase inverter-based distributed generation," *IEEE Trans. Power Del.*, vol. 24, no. 2, pp. 919–929, apr 2009.

[22] J. Kukkola, M. Hinkkanen, and K. Zenger, "Observer-based state-space current controller for a grid converter equipped with an LCL filter: Analytical method for direct discrete-time design," *IEEE Trans. Ind. Appl.*, vol. 51, no. 5, pp. 4079–4090, sep 2015.

[23] S. G. Parker, B. P. McGrath, and D. G. Holmes, "Regions of active damping control for LCL filters," *IEEE Trans. Ind. Appl.*, vol. 50, no. 1, pp. 424–432, jan 2014.

[24] J. Wang, J. D. Yan, L. Jiang, and J. Zou, "Delay-dependent stability of single-loop controlled grid-connected inverters with LCL filters," *IEEE Trans. Power Electron.*, vol. 31, no. 1, pp. 743–757, jan 2016.

[25] X. Wang, F. Blaabjerg, and P. C. Loh, "Passivity-based stability analysis and damping injection for multiparalleled vscs with lcl filters," *IEEE Trans. Power Electron.*, vol. 32, no. 11, pp. 8922–8935, 2017.

[26] J. Sun, "Impedance-based stability criterion for grid-connected inverters," *IEEE Trans. Power Electron.*, vol. 26, no. 11, pp. 3075–3078, 2011.

[27] D. Perez-Estevez, J. Doval-Gandoy, A. G. Yepes, and O. Lopez, "Positive- and negative-sequence current controller with direct discrete-time pole placement for grid-tied converters with LCL filter," *IEEE Trans. Power Electron.*, vol. 32, no. 9, pp. 7207–7221, sep 2017.

Jiancheng Zhao (Student Member, IEEE) obtained his B.S. in the School of Information Science and Engineering, Central South University, Changsha, China. He works for the Ph.D. on control science and engineering in the School of Automation Engineering, University of Electronic Science and Technology of China, Chengdu, China since 2016. His current research interests include voltage source inverter, microgrid, and motor control.

Chuan Xie (Senior Member, IEEE) received the B.S. degree in automation engineering from the University of Electronic Science and Technology of China (UESTC), Chengdu, China, and the Ph.D. degree in power electronics from Zhejiang University (ZJU), Hangzhou, China, in 2007 and 2012, respectively.

Since 2012, he was a Lecturer with the School of Automation Engineering at UESTC, where he was promoted as an Associate Professor in 2019. From May 2015 to May 2016, he was a Visiting Scholar at the Department of Energy Technology, Aalborg University (AAU). His main research interests include digital control of power electronics, grid synchronization technology, distributed generation systems, microgrids and power quality.

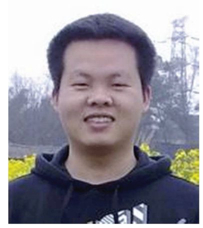

Kai Li (Member, IEEE) received the B.S., M.S., and Ph.D. in Automation Engineering from the University of Electronic Science and Technology of China, Chengdu, China in 2006, 2009, and 2014, respectively.

From 2009 to 2016, he was an Assistant Professor with the School of Automation Engineering, University of Electronic Science and Technology of China, Chengdu, China. From 2016.2 to 2017.2, he was an Guest Researcher with the Department of Energy Technology, Aalborg University, Denmark. Since 2016, he has been an Associate Professor with the School of Automation Engineering, University of Electronic Science and Technology of China, Chengdu, China. His research interests include multilevel inverters, storage converters, and microgrids.

Jianxiao Zou (Member, IEEE) received the B.S., M.S., and Ph.D. degrees in control science and engineering from the University of Electronic Science and Technology of China, Chengdu, China in 2000, 2003, and 2009, respectively.

He is currently a professor at University of Electronic Science and Technology of China (UESTC). He served as Vice Dean of School of Automation Engineering from 2011. He also served as the vice president of Sichuan Electrotechnical Society, vice president of Society for electrical engineering, and the Chairman of member development, Chengdu Section of IEEE China. He was a visiting scholar of University of California, Berkeley (UC Berkeley) in 2010 and senior visiting professor of Rutgers, The State University of New Jersey in 2014. He organized more than 10 international conferences/symposiums as general/program chairs and Session Chair. He has been publishing more than 50 journal papers and has been authorized more than 120 national invention patents. His research interests include control theory and control engineering, renewable energy control technologies, intelligent information processing and control.

Josep M. Guerrero (Fellow, IEEE) received the B.S. degree in telecommunications engineering, the M.S. degree in electronics engineering, and the Ph.D. degree in power electronics from the Technical University of Catalonia, Barcelona, in 1997, 2000 and 2003, respectively. Since 2011, he has been a Full Professor with the Department of Energy Technology, Aalborg University, Denmark, where he is responsible for the Microgrid Research Program. From 2012 he is a guest Professor at the Chinese Academy of Science and the Nanjing University of Aeronautics and Astronautics; from 2014 he is chair Professor in Shandong University; and from 2015 he is a distinguished guest Professor in Hunan University.

His research interests is oriented to different microgrid aspects, including power electronics, distributed energy-storage systems, hierarchical and cooperative control, energy management systems, and optimization of microgrids and islanded minigrids.